DE GRUYTER High Temperature Materials and Processes 2022; 41: 434–448

Research Article

Xinwang Wang, Li Fan*, Yurong Xu, Haiyan Chen*, Qizheng Cao, Lihua Dong, and Yujiang Qin

Low-temperature corrosion behavior of laser cladding metal-based alloy coatings on EH40 high-strength steel for icebreaker

https://doi.org/10.1515/htmp-2022-0042
received March 23, 2022; accepted May 17, 2022

Abstract: In this paper, four kinds of coatings Ni + 30% WC, Ni + 15% WC, Ni, and Co are prepared on EH40 steel by laser cladding technology. Electrochemical experiment tests at a simulating low-temperature (−40°C) environment in 0.5 $\text{mol}\cdot\text{L}^{-1}$ hydrochloric acid (HCl) solution and 3.5 wt% NaCl solution were conducted, and the polarization curve and electrochemical impedance spectroscopy (EIS) impedance spectrum were obtained. The results show that the Ni + 15% WC coating has the smallest corrosion current and 0.5 $\text{mol}\cdot\text{L}^{-1}$ HCl solution and 3.5 wt% NaCl solution have the maximum polarization resistance and impedance arc. Coatings will be treated in a 0.5 $\text{mol}\cdot\text{L}^{-1}$ HCl solution and 3.5 wt% NaCl solution at −40°C immersion for 30 days; finally, X-ray photoelectron spectroscopy (XPS) and scanning electron microscope (SEM) were used for test passivation films of Ni + 15% WC samples and sample surface morphology after corrosion. XPS results show that Fe, Mo, and Ni elements can form metal oxides in the 0.5 $\text{mol}\cdot\text{L}^{-1}$ HCl solution, and Cr, Fe, Mo, Ni, and W elements can form metal oxides in the 3.5 wt% NaCl solution. SEM results display that relatively severe corrosion appeared on the substrate near tungsten carbide in a 0.5 $\text{mol}\cdot\text{L}^{-1}$ HCl solution, and coating will be corroded form inside of the coating owing to the corrosive solution will penetrate the substrate. In 3.5 wt% NaCl solution, severe corrosion of the substrate has not been observed; however, the binding part has been obviously corroded.

Keywords: laser cladding coating, electrochemistry, passivation film, corrosion resistance, low temperature

1 Introduction

Under the background of global warming and the gradual melting of Arctic glaciers, the Arctic has an important strategic value in resources, shipping, and military affairs. At the same time, due to the rich oil, natural gas, and other mineral resources, more and more countries pay attention to the development and governance of the polar regions. However, less attention has been paid to research studies on materials suitable for the polar environment. EH40 steel is a structural material for icebreaker, because of its good mechanical properties and electrochemical corrosion resistance, especially the yield strength and tensile strength are high, and impact energy is low in the low temperature (−20 and −40°C) [1]. However, when used for icebreaker hull at low temperature, its low-temperature wear resistance and corrosion resistance are relatively poor.

In recent years, ceramics and metal matrix composite were deposited on the base steel surface to form the protective layer by laser cladding technology, which has been extensively used by researchers [2,3]. At present, ceramics reinforcing particles include titanium carbide (TiC) [4,5], tungsten carbide (WC) [6,7], niobium carbide (NbC) [8,9], and boride [10,11], and metal matrix composite contains iron-based alloy [12,13], cobalt-based alloy [14,15], and nickel-based alloy [16,17]. According to the previous research, due to the corrosion resistance of WC ceramic particles, the addition of WC reinforcing particles will improve the corrosion resistance of nickel-based coating [18,19]; the paper shows that the polarization resistance will increase from 3,435 to 11,902 $\Omega\cdot\text{cm}^2$ with the increase of WC content in the 0.05 $\text{mol}\cdot\text{L}^{-1}$ NaCl solution, which means that the appropriate WC content is

---

*** Corresponding author: Li Fan,** College of Mechanical and Electronic Engineering, Shanghai Jian Qiao University, Shanghai 201306, China, e-mail: 18126@gench.edu.cn
*** Corresponding author: Haiyan Chen,** College of Ocean Science and Engineering, Shanghai Maritime University, Shanghai 201306, China, e-mail: hychen@shmtu.edu.cn
Xinwang Wang, Yurong Xu, Qizheng Cao, Lihua Dong: College of Ocean Science and Engineering, Shanghai Maritime University, Shanghai 201306, China
Yujiang Qin: College of Mechanical and Electronic Engineering, Shanghai Jian Qiao University, Shanghai 201306, China

Table 1: Chemical composition of EH40 steel (wt%)

Elements	P	S	C	Cr	Si	Mn	Mo	V	Ni	Cu	Fe
Content	0.010	0.0015	0.16	0.20	0.15	0.90	0.08	0.10	0.40	0.35	Bal.

beneficial to corrosion resistance. At present, the effect of WC shape and particle and diameter on nickel-based coating performance was studied; Hochstrasser et al. [20] researches that the corrosion behavior of cobalt-based WC coating in the various pH value, and the study reveals that the cobalt-based binder phase will be corroded when pH is less than 7, adversely WC will be corroded when pH is greater than 7. Otherwise, some researchers are concerned about the corrosion behavior of alloy coatings in different acidic environments. Kim et al. [21] reveals that Co will react with other elements and form a uniform and continuous rust layer such as Fe, O, and S in a 10 wt% sulfuric acid solution at room temperature.

At present, researchers pay little attention to the corrosion performance of Ni-based tungsten carbide composite coating at low temperatures. This paper focuses on the corrosion behavior of nickel-based spherical tungsten carbide coatings in low temperatures and different corrosive environments. Polarization curve and EIS tests were carried out in simulated low temperature (−40°C) in both 0.5 mol·L^{-1} hydrochloric acid (HCl) and 3.5 wt% NaCl solutions. The characteristics of passive film formed on the as-received composite coatings were emphasized and characterized by X-ray photoelectron spectroscopy (XPS) measurement. This study can provide experimental data for further application of such developed Ni-based tungsten carbide composite coatings in the polar regions.

2 Experimental materials and methods

2.1 Experimental materials

EH40 marine steel was used as the substrate steel of the experiment, its size is 300 mm × 300 mm × 40 mm, and its chemical composition is given in Table 1. Nickel-based powder and cast spherical tungsten carbide powder were used as laser cladding powder. The chemical composition of nickel-based powder is shown in Table 2, and cobalt-based powder is presented in Table 3.

Table 2: Chemical composition of nickel-based powder (wt%)

C	P	Mo	W	Fe	Mn	Cr	Si	O	V	Ni
0.12	0.016	15.9	4.5	2.9	1.3	15.6	0.6	0.03	0.6	Bal

First, nickel-based alloy powder and WC powder were mixed according to the experimental ratio, and the added mass ratio of reinforced WC particles in the Ni/WC composite powders are 0, 15, 30 wt%, and the pure cobalt-based coating. Then, four mixed powders were coated on the surface of EH40 high-strength steel to form four coatings. Compositions of the studied coating are shown in Table 4.

The four as-received coatings were cut into 10 mm × 10 mm × 5 mm by wire cutting and then polished with sandpaper to conduct an electrochemistry experiment. The solution for the immersion experiment is 0.5 mol·L^{-1} HCl solution and 3.5 wt% sodium chloride (NaCl) solution at −40°C. The immersion time is 30 days. After reaching the predetermined time, the samples were taken out and used for EIS and polarization curve tests. Some samples were cut into 5 mm × 5 mm × 2 mm with wire cutting for the XPS test. Then, the surface morphology after corrosion was observed by a scanning electron microscope (SEM).

2.2 Electrochemical performance test

The size of the electrochemical test sample is 10 mm × 10 mm × 5 mm. It is polished with sandpaper, and the opposite side of the test surface is connected with copper wire and then sealed with epoxy resin. The packaged

Table 3: Chemical composition of cobalt-based powder (wt%)

Mo	W	Ni	Fe	Cr	Si	C	Co
6	2.5	10	3.5	28	1	0.1	Bal.

Table 4: Compositions of the studied coatings

Specimen	Compositions (wt%)		
	Co	Ni	WC
Ni + 30% WC	0	70	30
Ni + 15% WC	0	85	15
Ni	0	100	0
Co	100	0	0

samples were immersed in 0.5 mol·L^{-1} HCl and 3.5 wt% NaCl solution, respectively, and placed in a low-temperature environment of −20°C for 120 h. When the predetermined time is reached, the sample is taken out and put in room temperature HCl and NaCl solution for the polarization curve and EIS test. The polarization curve and EIS test use a three-electrode electrochemical workstation (CHI 660): a saturated calomel electrode and a platinum plate are used as the reference electrode and an auxiliary electrode, respectively. Polarization resistance, corrosion potential, and corrosion current are obtained by the polarization curve test.

2.3 Characterization of the passive films

The size of the XPS sample is 5 mm × 5 mm × 2 mm. It is immersed in HCl and NaCl solution for 240 and 360 h, respectively. Then, the passive film was tested by XPS, and the relationship between the electrochemical test results and the surface morphology of the coating was revealed. The XPS test instrument ESCALAB 250Xi is manufactured by Thermo Fisher Scientific), the X-ray source is a monochromatic Al target (1486.6 eV), the scanning mode of the energy analyzer is CAE, the C1s external standard method is used to correct the energy spectrum, and the XPSPEAK software is used to fit the results.

3 Results and discussion

3.1 Microstructure and phase composition of the coating

Figure 1 shows the X-ray powder diffraction patterns of the three coatings. During the laser melting process, the surface of the substrate steel and the nickel-based alloy powder is melted at high temperature, forming a molten pool in a tiny area. The vibration amplitude becomes larger, so that some atoms escape from the original lattice, enter the holes or lattice gaps of other material lattices, and form a γ-Ni solid solution. At the same time, in the high-temperature environment, some metal substances will react with free carbon to form new compounds, and the newly formed carbides will also enter the lattice of nickel. The XRD analysis of the Ni coating shows that the nickel-based alloy coating has two solid solution phases, γ-Fe and γ-Ni. The reason for the formation of these two solid solutions is that the high temperature during the laser cladding process melts the nickel-based alloy powder. The powder melted at high temperature will be rapidly cooled and recrystallized in the molten pool, and some Mo and W atoms will remain in the Ni lattice and Fe lattice. The formation of γ-Fe and γ-Ni solid solutions with some Mo and W atoms will greatly improve the strength and hardness of the coatings. In addition to the composition of γ-Ni itself, the phase of Ni + 15% WC coating also forms Ni_4W and Cr_2Ni_3 compounds with W, Cr, and Ni. In addition, under the action of high temperature, carbon atoms will also react with Fe, Ni, and Cr to form carbides ($M_{23}C_6$). The analysis of Ni + 30% WC coating by XRD shows that atoms such as Cr, Mo, and W will enter into the nickel lattice, and the solid solutions in the coating mainly include γ-Ni, Ni_4W, Cr_2Ni_3, and other solid solutions. At the same time, metal atoms M will react with carbon atoms to produce carbides ($M_{23}C_6$). Because the diffraction peaks of WC and W_2C were not found in the XRD diffraction pattern, the diffraction peaks of carbide ($M_{23}C_6$) and Ni_4W solid solution increased with the increase of the content of tungsten carbide. Carbide ($M_{23}C_6$) and Ni_4W compounds are hard phases, and their hardness is greater than that of the coating matrix, so it is beneficial to improve the corrosion resistance of the coating.

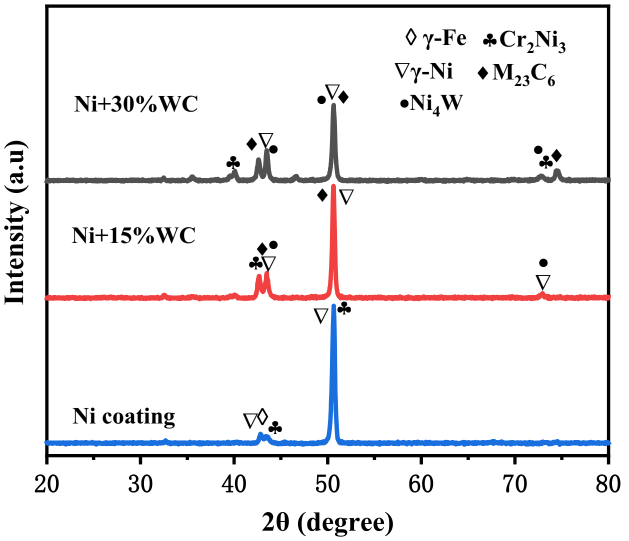

Figure 1: XRD spectra of pure Ni coating and Ni-based coatings with WC added.

Figure 2 shows the SEM image of the three coating samples. It can be seen from Figure 2 that the microstructure of the Ni coating is relatively uniform, and there are no obvious coating defects. However, there are some pores and holes on Ni + 30% WC coating and Ni + 15% WC coating. The main reason for the formation of holes and cracks is that during the solidification of the molten

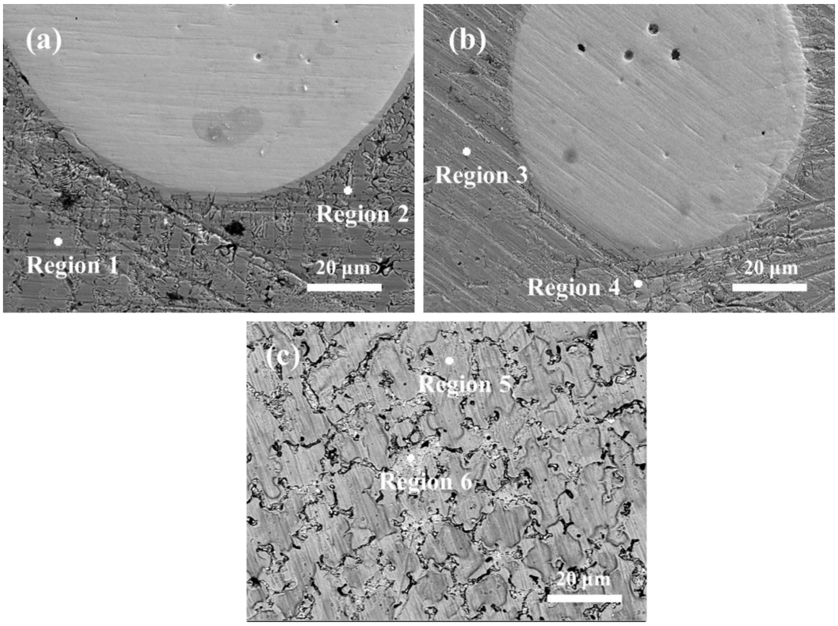

Figure 2: Surface SEM of composite coatings: (a) Ni + 30% WC; (b) Ni + 15% WC; (c) Ni.

pool, the flow of the molten pool is inhibited by the tungsten carbide, resulting in the gas trapped in the molten pool; the third is due to the thermal expansion coefficient of the tungsten carbide and the binder phase material is different [22–24]. The corresponding energy dispersive spectroscopy (EDS) analyses are shown in Figure 3. The Ni + 30% WC coating also contains a large number of complex precipitation phases. The structure of this region is a relatively fine dendritic structure, and the growth direction is relative to the tungsten carbide particles. The main reason for the formation of dendrites is the formation of carbides by atoms such as carbon, molybdenum, and tungsten. The microstructure of the Ni + 15% WC coating sample is relatively coarse, with both coarse dendritic structure and flaky structure, and holes of different sizes are also distributed on the surface of the structure. There are a lot of carbon, chromium, nickel, and other elements; the precipitation products in this area are $M_{23}C_6$, NiW_4, and Cr_2Ni_3. The microstructure of the Ni-based coating is finer and uniform, without obvious coating defects, and the hard phase is mainly composed of dendrites and interdendritic structures. It is mainly composed of γ-Ni solid solution and Cr_2Ni_3.

3.2 Potentiodynamic polarization behavior

Figure 4a shows the polarization curves of different coatings in HCl solution, and Figure 4b shows the polarization curves of different coatings in NaCl solution. Figure 4a shows that the four coatings have obvious passivation phenomena. According to the polarization curve, it can be seen that the passivation range is between −0.2 and 0 V. With the increase of WC content, the passivation phenomenon will become obvious, and then the passivation phenomenon will be slow down, that is, the passivation phenomenon of Ni + 15% WC coating is the most obvious. Figure 4b shows that the Co coating has no obvious passivation, and the other three coatings have passivation in NaCl solution, which is similar to corrosion in HCl solution. The passivation film is in the range of −0.2 to 0 V, with the increase of WC, the passivation phenomenon becomes obvious and then slows down. According to recent studies [25,26], when metal alloy corrosion occurs in a solution, the metal loses electrons and forms metal ions. Considering the oxygen dissolved in the solution, it will form dense metal oxides in the solution and adsorb on the metal surface, such as Cr_2O_3, MoO_2, WO_3, NiO, etc. The formation of dense metal oxides can effectively slow down corrosion [27].

The polarization curve test can be used to fit parameters such as corrosion potential E_{corr}, corrosion current i_{corr}, etc. Table 5 shows the polarization curve fitting results of 0.5 mol·L^{-1} HCl solution. It can be seen from Table 5 that as the WC content increases, the corrosion potential of the sample gradually moves positively. The reason for this phenomenon is that WC is ceramic particles, which have strong corrosion resistance, but there is galvanic corrosion between WC and the metal bonding phase. Excessive tungsten carbide content will aggravate

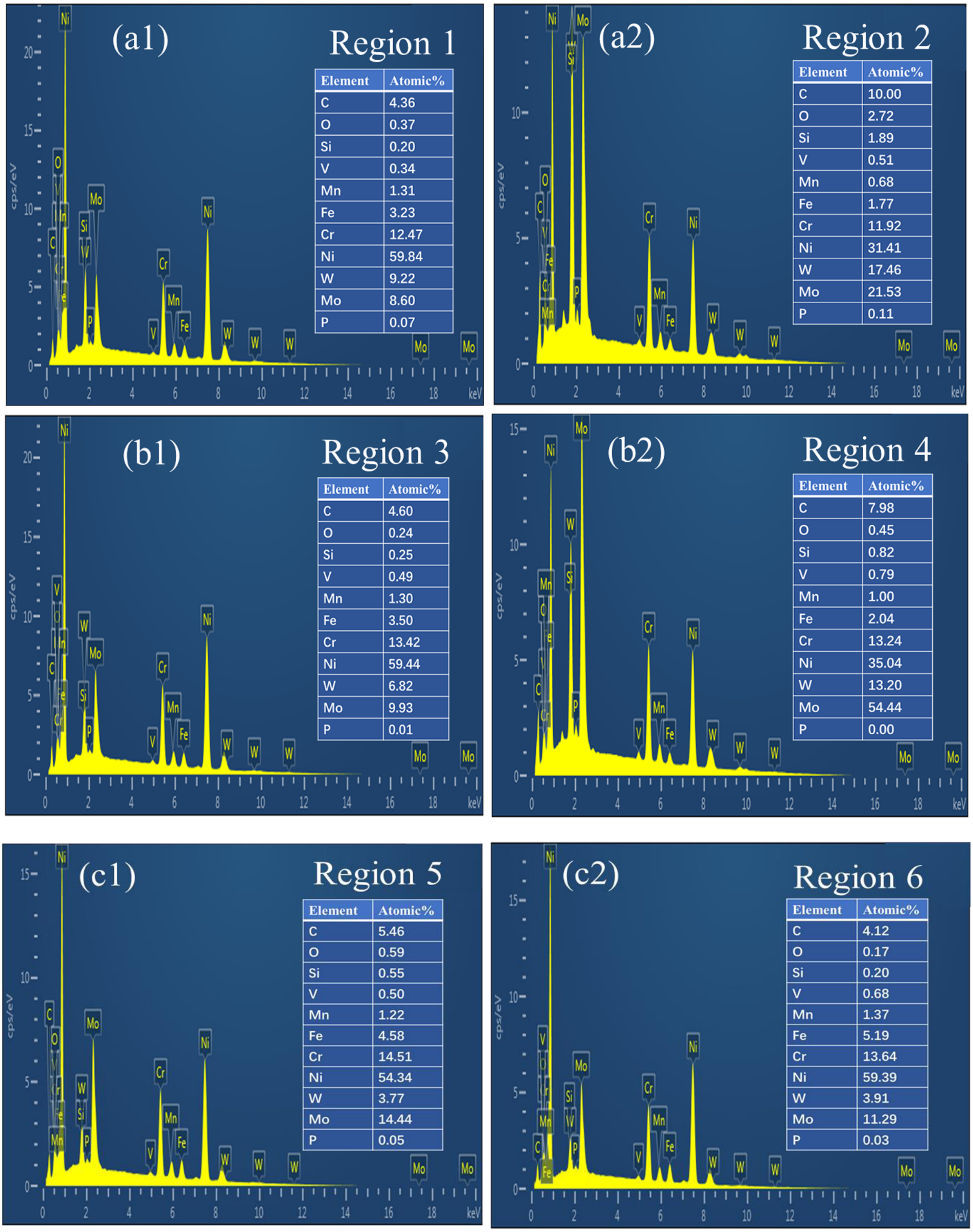

(a1) Region 1

Element	Atomic%
C	4.36
O	0.37
Si	0.20
V	0.34
Mn	1.31
Fe	3.23
Cr	12.47
Ni	59.84
W	9.22
Mo	8.60
P	0.07

(a2) Region 2

Element	Atomic%
C	10.00
O	2.72
Si	1.89
V	0.51
Mn	0.68
Fe	1.77
Cr	11.92
Ni	31.41
W	17.46
Mo	21.53
P	0.11

(b1) Region 3

Element	Atomic%
C	4.60
O	0.24
Si	0.25
V	0.49
Mn	1.30
Fe	3.50
Cr	13.42
Ni	59.44
W	6.82
Mo	9.93
P	0.01

(b2) Region 4

Element	Atomic%
C	7.98
O	0.45
Si	0.82
V	0.79
Mn	1.00
Fe	2.04
Cr	13.24
Ni	35.04
W	13.20
Mo	54.44
P	0.00

(c1) Region 5

Element	Atomic%
C	5.46
O	0.59
Si	0.55
V	0.50
Mn	1.22
Fe	4.58
Cr	14.51
Ni	54.34
W	3.77
Mo	14.44
P	0.05

(c2) Region 6

Element	Atomic%
C	4.12
O	0.17
Si	0.20
V	0.68
Mn	1.37
Fe	5.19
Cr	13.64
Ni	59.39
W	3.91
Mo	11.29
P	0.03

Figure 3: EDS results of different regions in Figure 2: (a1) and (a2) Ni + 30% WC; (b1) and (b2) Ni + 15% WC; (c1) and (c2) Ni coating.

galvanic corrosion. Usually, the potential is more positive, the tendency of corrosion is smaller. The corrosion potentials of Ni + 30% WC and Ni + 15% WC samples are −308 and −315 mV, respectively, which are significantly higher than Ni (−347 mV). The corrosion potential of the Co sample is −342 mV; owing to its natural chemical, the

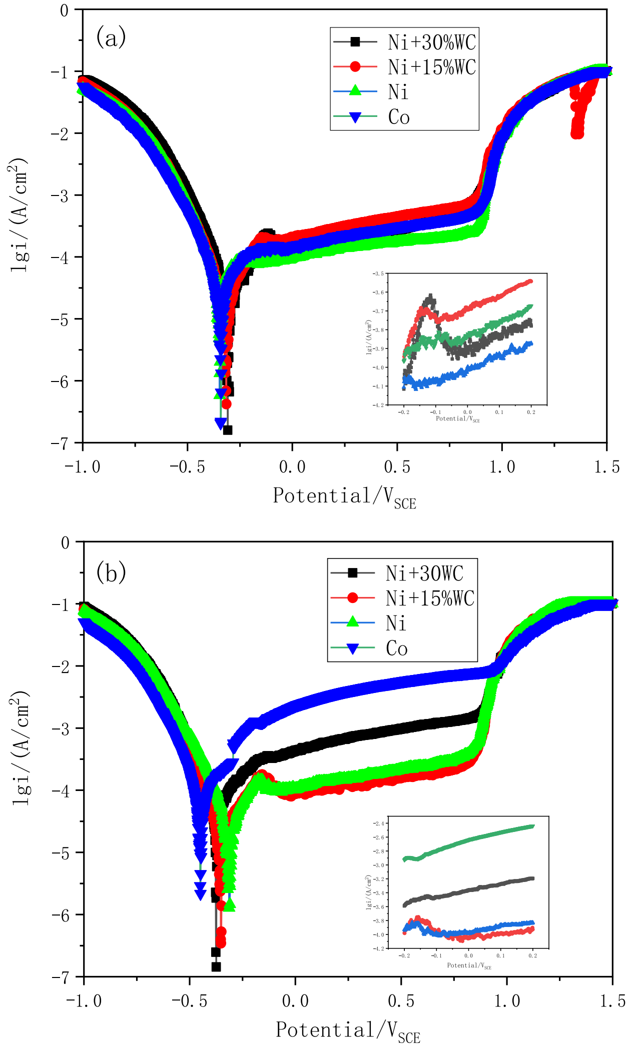

Figure 4: Potential polarization curve of different coatings in the 0.5 mol·L^{-1} HCl solution (a) and 3.5 wt% NaCl solution (b) for 120 h.

corrosion potential is more negative than Ni. In Table 5, βa, βc, and R_p are anode slope, cathode slope, and polarization resistance, respectively. The anode slopes of the four coatings are significantly larger than the cathode slope, indicating that the anode process resistance is greater than the cathode process resistance, and the corrosion process is mainly controlled by the anode process. From a dynamic point of view, the larger the polarization resistance R_p and the smaller the corrosion current i_{corr} indicates that the corrosion resistance of the sample is better. The order of the polarization resistance is Ni + 15% WC (1357.6 Ω) > Ni + 30% WC (908.7 Ω) > Ni (875.3 Ω) > Co (853.5 Ω), the order of corrosion current is Ni + 15% WC (20.65 μA·cm^{-2}) < Ni (33.47 μA·cm^{-2}) < Ni + 30% WC (36.37 μA·cm^{-2}) < Co (38.44 μA·cm^{-2}).

Table 6 shows the polarization curve fitting results of 3.5 wt% NaCl solution. It can be seen from Table 6 that the slope of the anode is much larger than the slope of the cathode, which is the same as the corrosion in the HCl solution, and the surface corrosion process is controlled by the anode process. With the increase of WC content, the corrosion current density of the sample will first decrease and then increase, and the trend of polarization resistance is the same as current density. Relevant studies have shown that the coating process will cause cracks, holes, and other defects because of the different thermal expansion coefficients of WC particles and nickel-based alloys. The corrosion current of the Ni + 30% WC sample increases rapidly, and the polarization resistance is reduced, which may be related to the surface defects of the specimen [28–30]. This is why Ni + 15% WC has the smallest corrosion current in NaCl solution (25.14 μA·cm^{-2}) and the maximum polarization resistance (1303.5 Ω). In NaCl solution, the order of corrosion current density is Ni + 15% WC (25.14 μA·cm^{-2}) < Ni (28.39 μA·cm^{-2}) < Ni + 30% WC (112 μA·cm^{-2}) < Co (114.7 μA·cm^{-2}).

The above research [28–30] shows that the samples with 10–30% mass fraction of WC have fewer defects, and when the mass fraction of WC exceeds 30%, defects increase. In an acidic environment, there is galvanic corrosion between WC and the binder phase, which is the main cause of corrosion and dissolution of the binder phase. The increase of defects will aggravate galvanic corrosion. As the WC content increases, the corrosion performance will decrease. In a NaCl solution with a mass fraction of 3.5%, the corrosion performance will also decrease as the WC content increases.

Table 5: Corrosion parameters fitting results according to the potential dynamic polarization curves in 0.5 mol·L^{-1} HCl solution for 120 h

Specimen	E_{corr} (mV)	i_{corr} (μA·cm^{-2})	R_p (Ω)	βa (V·dec^{-1})	βc (V·dec^{-1})
Ni + 30% WC	−308	36.37	908.7	8.907	4.251
Ni + 15% WC	−315	20.65	1357.6	9.183	6.324
Ni	−347	33.47	875.3	7.281	1.573
Co	−342	38.44	853.5	8.520	4.732

Table 6: Corrosion parameters fitting results according to the potential dynamic polarization curves in 3.5 wt% NaCl solution for 120 h

Specimen	E_{corr} (mV)	i_{corr} (μA·cm^{-2})	R_p (Ω)	βa (V·dec^{-1})	βc (V·dec^{-1})
Ni + 30% WC	−374	112	366.1	7.829	3.314
Ni + 15% WC	−352	25.14	1303.5	8.651	4.614
Ni	−313	28.39	1088.4	8.490	5.579
Co	−449	114.70	356.1	7.411	3.238

3.3 Impedance spectra

The Nyquist of the four coatings is shown in Figure 5, and Figure 5a shows the Nyquist diagram of the coating in the 0.5 mol·L^{-1} HCl solution, which shows that the impedance spectra of the four coatings present a semicircular arc shape and only one capacitive reactance arc included, and the high-frequency capacitive reactance arc is closely related to the electron transfer process on the sample surface. The arc radius of the Ni + 15% WC sample is larger than that of other coating samples, indicating that Ni + 15% WC has the best impedance performance, which is consistent with the conclusion obtained from the polarization curve that the Ni + 15% WC coating has the best corrosion resistance. It can be observed from Figure 5a that in the HCl solution, the order of impedance of different coatings is Ni + 15% WC > Ni + 30% WC > Ni > Co.

Figure 5b shows the Nyquist diagram of the coating in the 3.5 wt% NaCl solution and shows that, compared with that in the HCl solution, the impedance arc radius of the Ni + 15% WC and Ni is relatively close, but the impedance arc radius of Ni + 30% WC coating in the 3.5 wt% NaCl solution is significantly reduced, the reason of the rapid decrease of the impedance arc of the Ni + 30% WC coating may be the defects in the coating. The defects of the Ni + 30% WC sample in the NaCl solution is shown in Figure 6. The impedance arc radius of Co coating is the smallest because of its lively chemical properties. It can be seen from Figure 5b that in the NaCl solution, the order of impedance of different coatings is Ni + 15% WC > Ni > Ni + 30% WC > Co. The arc radius of the Ni + 30% WC sample reduces rigidly because of the defects such as cracks and holes in the coating, which weakens the corrosion resistance of the coating, and the galvanic corrosion intensifies with the increase of WC content.

The Bode diagrams of the four coatings in different solutions are shown in Figure 7. Figure 7a shows the Bode diagram of different coatings in 0.5 mol·L^{-1} HCl solution. Figure 7a shows that the impedance of four coatings in the high-frequency region is about 1 Ω, and the phase angle is close to 0°, indicating that the solution impedance is about 1 Ω. In the middle-frequency region, the phase angle reaches the maximum, which is a typical capacitive reactance characteristic. In the low-frequency region, the capacitive reactance value is related to the electric double layer, and a platform appears in the low-frequency region, indicating that there are two time constants [31].

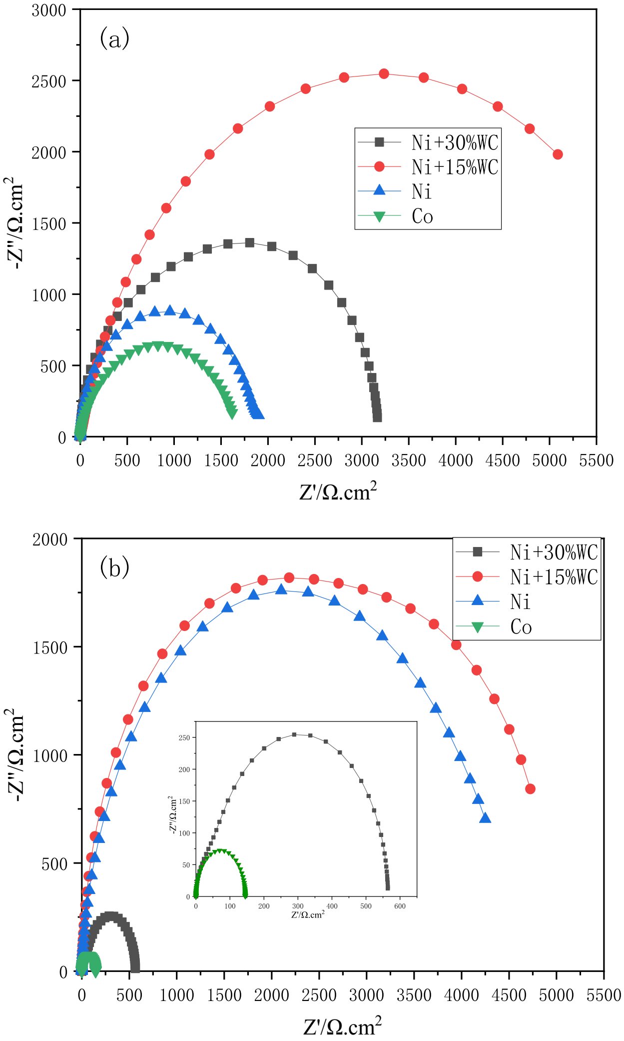

Figure 5: Nyquist plots of different coatings in the 0.5 mol·L^{-1} HCl solution (a) and 3.5 wt% NaCl solution (b) for 120 h.

Figure 7b shows the Bode diagram of different coatings in 3.5 wt% NaCl solution, and the Bode diagram also shows the characteristics of capacitive reactance. In the high-frequency region, the phase angle is close to 0°, indicating that the impedance is mainly solution resistance, and the impedance is about 1 Ω. In the low-frequency region, the coating impedance can reach 10,000 Ω due to the influence of the passivation film and the electric double layer. In the middle-frequency region, the phase angle reaches the maximum, which is a typical capacitive reactance characteristic.

Figure 8a shows the equivalent circuit of four coatings in 0.5 mol·L^{-1} HCl solution, and Figure 8b shows the equivalent circuit of four coating samples in the 3.5 wt% NaCl solution, where R_s is the solution resistance, R_f is the resistance of the passivation film, Q_f is the capacitive reactance of the passivation film, Q_{dl} is the electric double-layer capacitance, and R_{ct} is the electrochemical transfer resistance.

Fitting results of the circuit are shown in Table 7, where the capacitive reactance value of the Co sample is $1.164 \times 10^{-4}\ \Omega^{-1}\cdot\text{cm}^{-2}\cdot\text{s}^n$, and the passive film capacitive reactance of the Ni sample is $6.796 \times 10^{-5}\ \Omega^{-1}\cdot\text{cm}^{-2}\cdot\text{s}^n$. Due to the potential difference between WC and metal substrate, severe galvanic corrosion will occur at the binding part. When 15 wt% WC is added, the capacitive reactance value decreases to $2.208 \times 10^{-4}\ \Omega^{-1}\cdot\text{cm}^{-2}\cdot\text{s}^n$. When the mass fraction reaches 30%, the capacitive reactance value continues to decrease. R_{cf} is the electrochemical transfer resistance, and the electrochemical transfer resistance of the Ni + 15% WC sample is the largest. This indicates that the passivation film of the Ni + 15% WC sample has the best protective effect on the coating among the four coating samples. The R_{cf} value is related to the thickness of the passivation film and electric double layer. It can be seen from Table 7 that the transfer resistance of the Ni + 15% WC sample is the largest, reaching 6,321 Ω·cm^2, which is 3.1 times the transfer resistance of the Ni sample (1,994 Ω·cm^2), 1.3 times the Ni + 30% WC sample (4,633 Ω·cm^2). The results fitting the equivalent circuit show that the corrosion performance of Ni + 15% WC is the best, and the order of

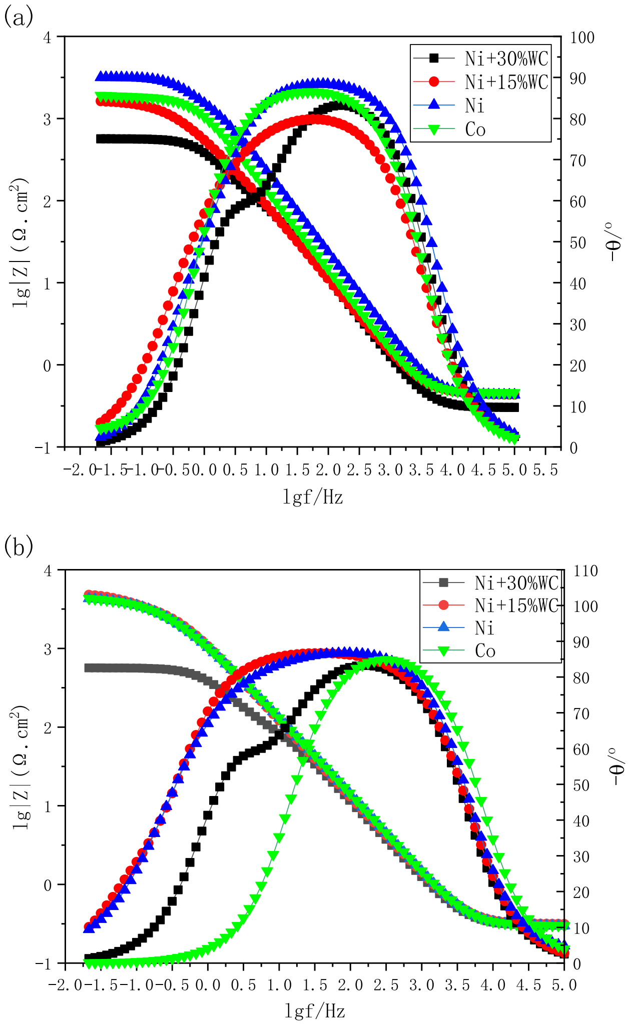

Figure 7: Bode impedance plots of different coatings in the 0.5 mol·L^{-1} HCl solution (a) and 3.5 wt% NaCl solution (b) for 120 h.

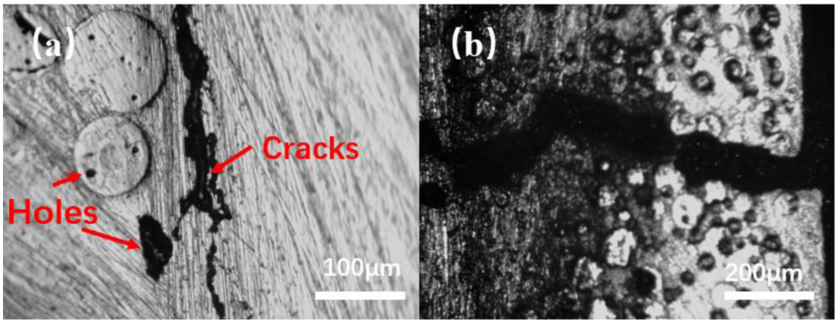

Figure 6: Surface (a) and cross section (b) defects of Ni + 30% WC sample coating in the 3.5 wt% NaCl solution.

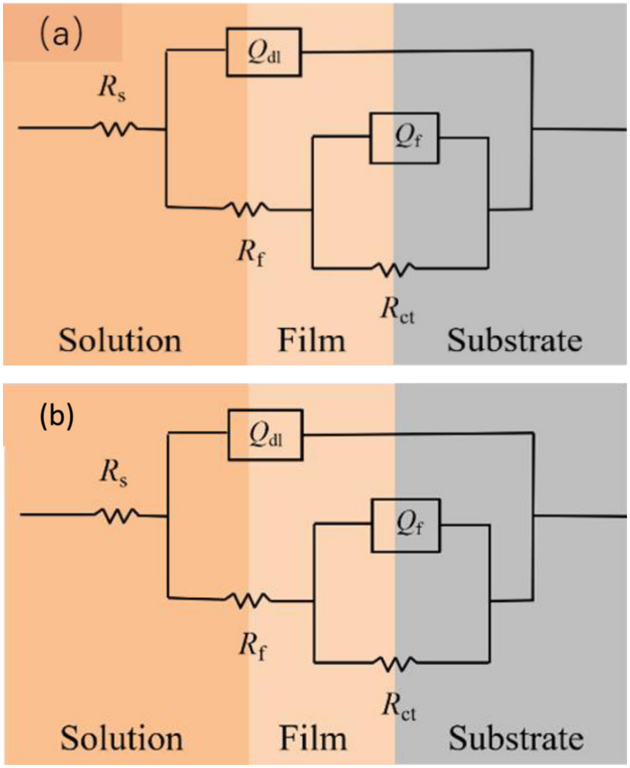

Figure 8: Equivalent circuit of EIS for coatings (a) in 5 mol·L^{-1} HCl solution and equivalent circuit of EIS for coatings in 3.5 wt% NaCl solution for 120 h.

corrosion performance is Ni + 15% WC > Ni + 30% WC > Ni > Co.

The results in Table 8 are obtained by fitting the circuit in Figure 8b. From the results in Table 8, the capacitive reactance value of the Ni passivation film is the smallest, which is 9.45 × 10^{-5} Ω^{-1}·cm^{-2}·s^{n}, and the resistance R_f is 2,106 Ω·cm^2. As the content of WC increases, the capacitive reactance value of the passivation film becomes smaller. Tungsten carbide is the noble particle that exhibits noble behavior in the corrosive environment than the nickel field. In the process of electrochemical corrosion, a microcell will be formed between the ceramic phase with high potential and the nickel-based alloy phase with low potential, resulting in galvanic corrosion during the thermal reaction, which makes the nickel-based alloy phase around these ceramic phases preferentially corroded in the process of electrochemical corrosion. This also proves that when the additional amount is 30% WC, the corrosion potential becomes relatively lower, and the self-corrosion current density becomes higher [32,33]. The transfer resistance R_{ct} has an obstructive effect on the entire charge transfer process. The transfer resistance of the Ni + 15% WC sample is the largest, reaching 4,127 Ω·cm^2, which is 1.1 times the transfer resistance of the Ni sample (3,739 Ω·cm^2) and 4.1 times that of the Ni + 30% WC sample (392.5 Ω·cm^2). Compared with other coatings, the transfer resistance of the Co sample in the NaCl solution is the smallest, which is 101.8 Ω·cm^2. The basic corrosion process for metallic components in an aqueous solution consists of the anodic dissolution of metals and the cathodic reduction of oxidants presented in the solution. In the branch of anodic polarization curves, the current densities increased exponentially at the initial stage. The corrosive mechanisms were an indication of being charge-transfer controlled. The current densities originated exclusively from the oxidation of the binder phase on the surface because of the standard potential for nickel oxidation (E_0 = −491 mV). This increase was caused by the formation and dissolution of a low valence oxide film, such as NiO, the step increase in the current densities could be caused by the oxidation of WC [34].

3.4 Surface analysis of Ni/WC coating after corrosion

Relevant studies have shown [35,36] that at the initial stage of corrosion, Cl$^-$ is adsorbed on the metal surface to produce corrosion. The anode metal will dissolve to form metal cations, which will combine O^{2-} and OH$^-$ in the solution to form a dense passivation film. With the increase of the adhesion of the passivation film, the

Table 7: Impedance fitting results of coating in 0.5 mol·L^{-1} HCl solution for 120 h

Specimen	R_s (Ω·cm^2)	Q_f		R_f (Ω·cm^2)	Q_{dl}		R_{ct} (Ω·cm^2)
		Y_0 (Ω^{-1}·cm^{-2}·s^{n})	n_f		Y_0 (Ω^{-1}·cm^{-2}·s^{n})	n_{dl}	
Ni + 30% WC	0.4829	2.65 × 10^{-4}	0.8845	573.6	2.149 × 10^{-4}	0.8075	4,633
Ni + 15% WC	0.4833	2.208 × 10^{-4}	0.9	769.4	1.652 × 10^{-4}	0.8	6,321
Ni	0.4293	6.796 × 10^{-5}	1	2,106	2.710 × 10^{-4}	1	1,994
Co	0.4685	1.164 × 10^{-4}	0.9888	1,515	5.658 × 10^{-2}	1	1,356

Table 8: Impedance fitting results of coatings in 3.5 wt% NaCl solution for 120 h

Specimen	R_s ($\Omega \cdot cm^2$)	Q_f		R_f ($\Omega \cdot cm^2$)	Q_{dl}		R_{ct} ($\Omega \cdot cm^2$)
		Y_0 ($\Omega^{-1} cm^{-2} \cdot s^n$)	n_f		Y_0 ($\Omega^{-1} \cdot cm^{-2} \cdot s^n$)	n_{dl}	
Ni + 30% WC	0.3018	1.597×10^{-4}	1	172.3	2.583×10^{-4}	1	392.5
Ni + 15% WC	0.3142	1.45×10^{-4}	1	3,571	1.453×10^{-3}	1	4,127
Ni	0.044	9.45×10^{-5}	0.6	2,648	1.076×10^{-4}	1	3,739
Co	0.2949	7.745×10^{-5}	1	115.3	1.731×10^{-2}	0.4193	101.8

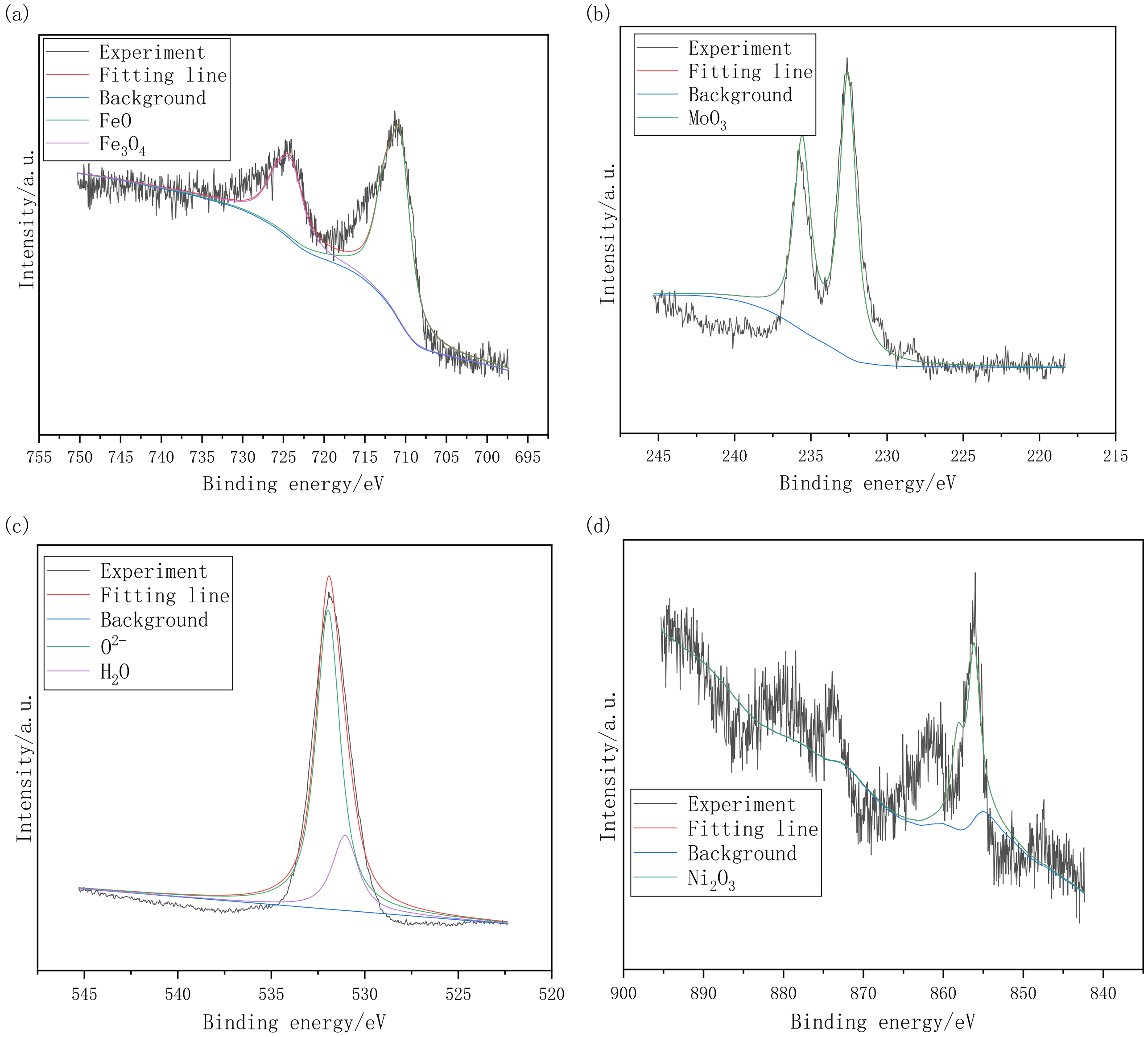

Figure 9: Fe (a), Mo (b), O (c) and Ni (d) high resolution XPS spectra of passive film of Ni + 15% WC coating exposed to 0.5 mol·L^{-1} HCl solution for 30 days.

passivation film effectively slows down the corrosion effect of Cl$^-$ and protects the anode metal material, indicating that the corrosion resistance of the sample has been improved.

Figure 9 reveals that after immersing in a 0.5 mol·L^{-1} HCl solution for 30 days, the passivation film on the surface of the sample is mainly stable in the form of oxides, hydroxides, and hydrates of different valence states of Fe, Ni, O, and Mo elements. The Fe2p spectrum contains the peak of Fe_3O_4 (723.9 eV) and FeO (710.6 eV); the Mo3d spectrum contains the peak of MoO_3 (232.5 eV); the Ni2p spectrum contains the peak of Ni_2O_3 (855.0 eV); the O1s spectrum is divided into two peaks, namely, the peak of H_2O (530.6 eV) and the O^{2-} peak (531.6 eV).

Figure 10 shows that the low and high magnified surface corrosion SEM images of Ni/WC coating exposed to 0.5 mol·L^{-1} HCl solution for 30 days. An obvious corrosion phenomenon has not been observed in Figure 10a, and Figure 10a1 shows a small amount of pit appearing on the coating surface. But Figure 10a2 displays that relatively severe corrosion occurs on the substrate near tungsten carbide, which is owing to the potential difference between tungsten carbide and the substrate, which will cause severe galvanic corrosion, and the substrate will be preferentially corroded due to low potential. Area 3 in Figure 10a2 is observed by high magnification SEM. Figure 10b and c show that pits and cracks appear after corrosion, which means that corrosive solution will penetrate the substrate, and the coating will corrode from inside of the coating. Due to the dissolution of Cr, Ni, and Mo, metal cation will combine with oxygen anion to form a metal oxide and adhere to the surface of the substrate, which is beneficial for corrosion resistance.

Figure 11 shows the XPS spectra of a Ni + 15% WC sample immersed in 3.5 wt% NaCl solution for 30 days. The spectrum has been processed with Shirley's background, and the main peaks are divided according to the XPS manual peak. The Cr2p spectrum is mainly composed of the peak of $Cr(OH)_3$ (586.3 eV), the peak of Cr_2O_3 (575.1 eV), and the peak of Cr (577.0 eV) (33); the O1s

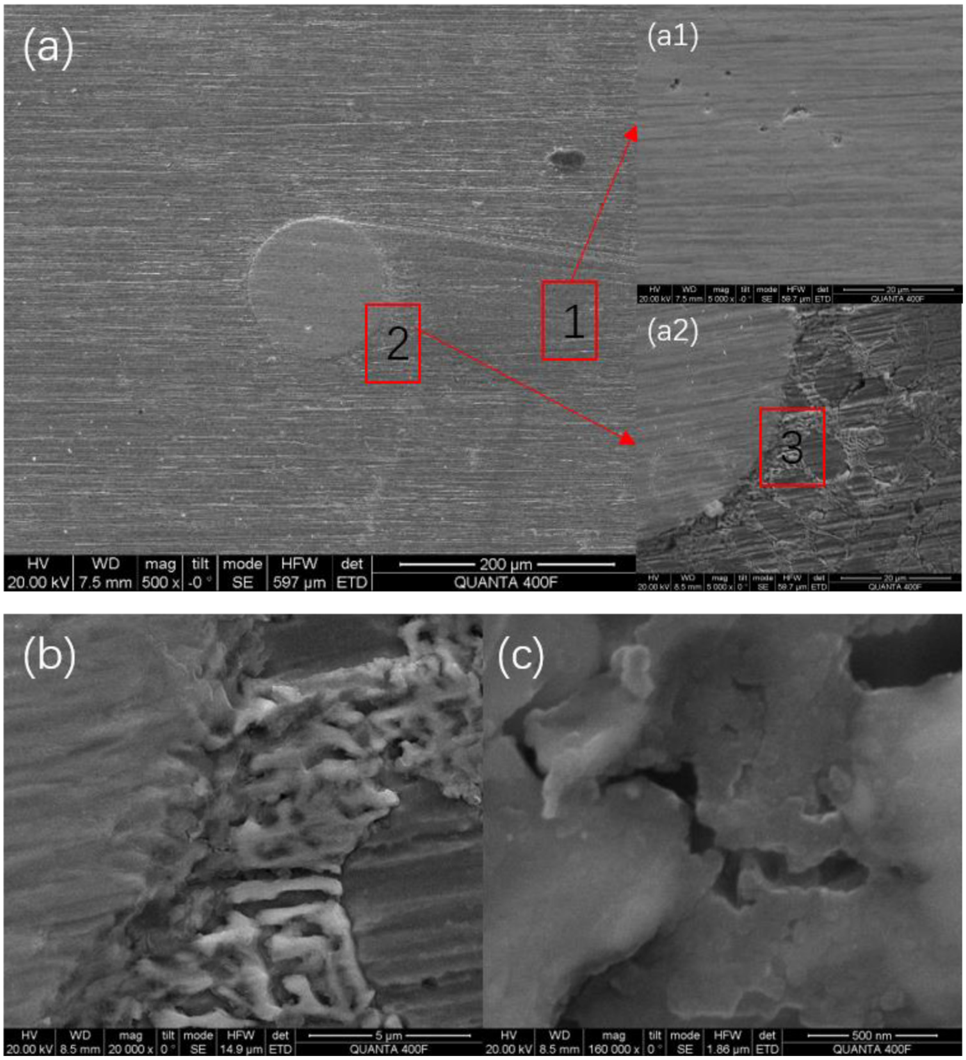

Figure 10: Low (a) and high (b and c) magnified surface corrosion SEM images of Ni/WC coating exposed to 0.5 mol·L^{-1} HCl solution for 30 days.

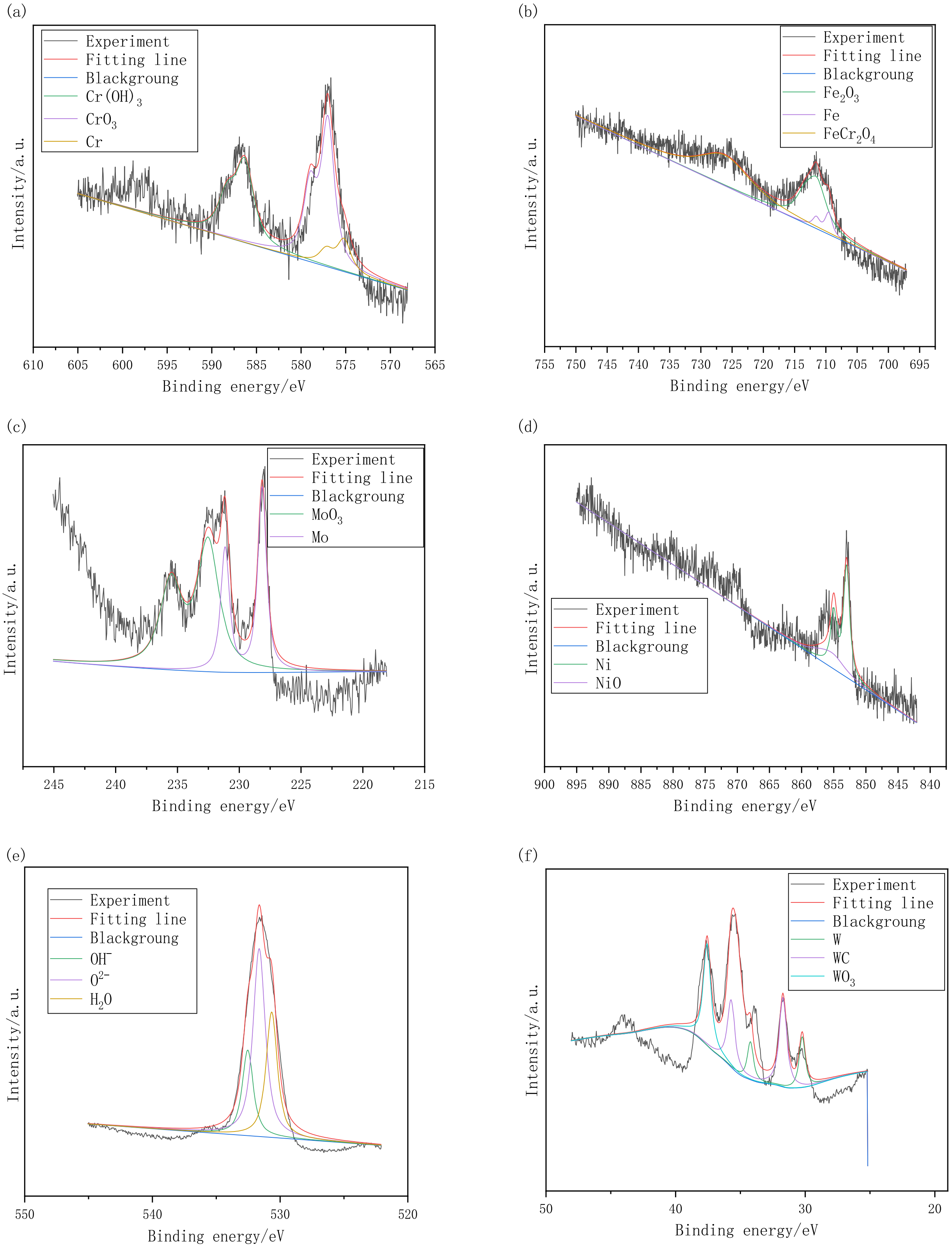

Figure 11: Cr (a), Fe (b), Mo (c), Ni (d), O (e) and W (f) high resolution XPS spectra of passive film of Ni + 15% WC coating exposed to 3.5 wt% NaCl solution for 30 days.

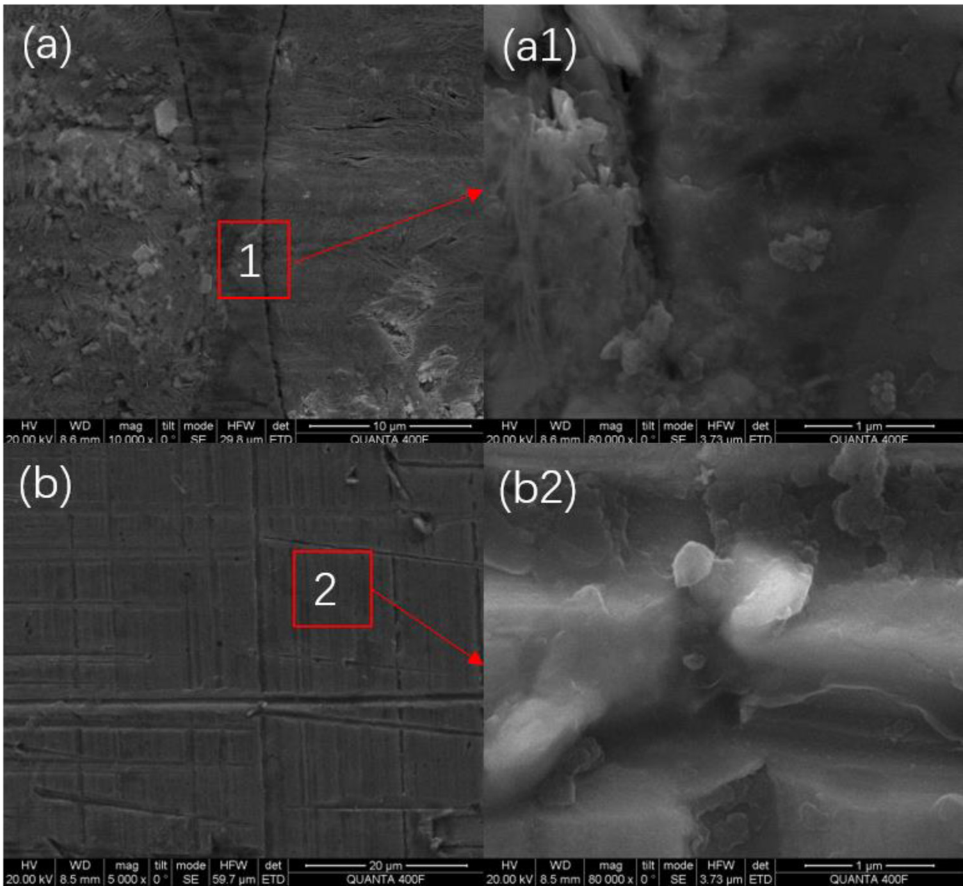

Figure 12: Low (a, b) and high (a1, b2) magnified surface corrosion SEM images of Ni/WC coating exposed to 3.5 wt% NaCl solution for 30 days.

spectrum is divided into three peaks, namely, the peak of H_2O (530.6 eV), O^{2-} peak (531.6 eV), and OH^- peak (532.5 eV) (15); the Fe2p spectrum contains the peak of Fe_2O_3 (711.4 eV), $FeCr_2O_4$ (725.5 eV), and Fe (709.5 eV); the Mo3d spectrum contains the peak of Mo (228.1 eV) and MoO_3 (232.5 eV); the Ni2p spectrum contain the peak of Ni (853.0 eV) and NiO (855.0 eV); W4f spectrum contain the peak of W (31.7 eV) and WO_3 (35.3 eV). The electrode potential of metal moves in the positive direction and decreases. It may be due to the formation of an oxide film that hinders the anodic reaction. Through XPS analysis, Ni_2O_3, MoO_3, and other oxides and $Cr(OH)_3$ hydroxides on the coating surface. According to the adsorption theory, oxygen is adsorbed on the surface of the alloy coating, and part of the oxygen is polarized by the electron couple in the metal, which reduces the activity of the anode and hinders the progress of the anode reaction [37].

Figure 12 shows high magnified surface corrosion SEM images of Ni/WC coating exposed to 3.5 wt% NaCl solution for 30 days. Figure 12 shows that there are obvious cracks between tungsten carbide and the substrate, resulting in the penetration of the corrosive solution into the cracks and severe corrosion. Figure 12a1 displays that lots of metal oxide hydroxide adhere to the surface of the substrate. Under the combined action of metal oxide and potential difference, the corrosion of the binding part is so serious that obvious cracks appear. Figure 12b shows that severe corrosion has not been observed on the surface of the substrate. Observing area 2 in Figure 12b, as shown in Figure 12b2, abundant metal oxide hydroxide adhering on the substrate surface, which can effectively delay corrosion of the substrate surface.

4 Conclusions

(1) According to the polarization curve fitting results, in the 0.5 mol·L^{-1} HCl solution, Ni + 15% WC has the smallest corrosion current (20.65 μA·cm^{-2}), the maximum polarization resistance (1357.6 Ω). In 3.5 wt%

NaCl solution, Ni + 15% WC also has the smallest corrosion current (25.14 $\mu A \cdot cm^{-2}$) and the maximum polarization resistance (1303.5 Ω).

(2) Electrochemical impedance spectroscopy (EIS) shows that the coating exhibits high-frequency impedance in both 0.5 $mol \cdot L^{-1}$ HCl solution and 3.5 wt% NaCl solution. In the two different solutions, the radius of the Ni + 15% WC impedance arc is the largest. The results of circuit fitting show that in HCl solution, the electrochemical transfer resistance of Ni + 15% WC is the largest, which is 6,321 $\Omega \cdot cm^2$; in NaCl solution, the electrochemical transfer resistance of Ni + 15% WC is the largest, which is 4,127 $\Omega \cdot cm^2$.

(3) XPS results show that Fe, Mo, and Ni elements can form metal oxides in 0.5 $mol \cdot L^{-1}$ HCl solution, and Cr, Fe, Mo, Ni, and W elements can form metal oxides in 3.5 wt% NaCl solution. Metal oxide and hydroxide adhering to the substrate surface can effectively delay corrosion of the substrate surface.

(4) In 0.5 $mol \cdot L^{-1}$ HCl solution, SEM results display that relatively severe corrosion appears on the substrate near tungsten carbide, and coating is corroded from inside of the coating owing to the penetration of the corrosive solution into the substrate. But in 3.5 wt% NaCl solution, severe corrosion of the substrate has not been observed; however, there is obvious corrosion in the binding part.

Acknowledgments: The authors gratefully acknowledge the fund support of Shanghai Maritime University and Shanghai Jian Qiao University.

Funding information: The authors gratefully acknowledge the support of the Shanghai special found (2019-jmrh1-kj45); Shanghai Engineering Technology Research Centre of Deep Offshore Material (19DZ2253100), and the Science & Technology Program of Shanghai Jian Qiao University (No. SJQ19012).

Author contributions: Xinwang Wang: writing – original draft, methodology, formal analysis; Li Fan: Writing – original draft, writing – review & editing, conceptualization, funding acquisition; Yurong Xu: resources, data curation, visualization; Haiyan Chen: writing – review & editing, conceptualization; Qizheng Cao: validation, data curation; Lihua Dong: conceptualization, funding acquisition, project administration; Yujiang Qin: validation, data curation.

Conflict of interest: Authors state no conflict of interest.

Data availability statement: The datasets generated during and analyzed during the current study are not publicly available due to data may be used in the next research, but are available from the corresponding author on reasonable request.

References

[1] Bian, S. Y., X. Zhang, S. L. Li, L. Zhang, W. J. Li, and L. Yan. Numerical Simulation, Microstructure, properties of EH40 ultra-heavy plate under gradient temperature rolling. *Materials Science and Engineering*, Vol. 791, 2020, id. 139778.

[2] Fernández, M. R., A. García, J. M. Cuetos, R. González, A. Noriega, and M. Cadenas. Effect of actual WC content on the reciprocating wear of a laser cladding NiCrBSi alloy reinforced with WC. *Wear*, Vol. 324–325, 2015, pp. 80–89.

[3] Shishkovsky, I., N. Kakovkina, and V. Sherbakov. Layerwise fabrication of refractory NiCrSiB composite with gradient grow of tungsten carbide additives by selective laser melting. *Optics and Laser Technology*, Vol. 120, 2019, id. 105723.

[4] Xiang, S. Q., S. F. Ren, Y. H. Liang, and X. F. Zhang. Fabrication of titanium carbide-reinforced iron matrix composites using electropulsing-assisted flash sintering. *Materials Science and Engineering*, Vol. 768, 2021, id. 138459.

[5] Damian, J. The friction and wear behaviour of in-situ titanium carbide reinforced composite layers manufactured on ductile cast iron by laser surface alloying. *Surface and Coatings Technology*, Vol. 406, 2021, id. 126634.

[6] Li, R. D., J. L. Li, Y. Liang, C. Z. Ji, and T. C. Yuan. Viscoplastic friction and microstructural evolution behavior of laser-clad Co-Cr-Ni-Mo coating. *Transactions of Nonferrous Metals Society*, Vol. 23, No. 3, 2013, pp. 681–691.

[7] He, R. G., J. Y. Wang, M. He, H. L. Yang, and J. M. Ruan. Synthesis of WC composite powder with nano-cobalt coatings and its application in WC-4Co cemented carbide. *Ceramics International*, Vol. 44, No. 9, 2018, pp. 10961–10967.

[8] Chang, S. H., L. Y. Hung, and T. H. Yang. The effects of adding micro-scaled niobium carbide on the microstructure, mechanical strength and polarization resistance of the Ti-8Mo-4Co-xNbC composites. *Materials Chemistry and Physics*, Vol. 235, 2019, id. 121743.

[9] Bian, Y., J. Ni, C. Wang, J. Zhen, H. Hao, X. Kong, et al. Microstructure and wear characteristics of in-situ micro/nanoscale niobium carbide reinforced copper composites fabricated through powder metallurgy. *Materials Characterization*, Vol. 172, 2021, id. 110847.

[10] Erdogan, A., A. Günen, M. S. Gök, and S. Zeytin. Microstructure and mechanical properties of borided $CoCrFeNiAl_{0.25}Ti_{0.5}$ high entropy alloy produced by powder metallurgy. *Vacuum*, Vol. 183, 2021, id. 109820.

[11] Zhu, Y. S., Y. F. Liu, X. N. Wei, D. Sun, W. Z. Lu, and T. J. Ko. Tribological characteristics of the dual titanium boride layers (TiB_2 + TiB) on titanium alloy. *Ceramics International*, Vol. 47, No. 10, 2021, pp. 13957–13969.

[12] Lin, T. J., H. H. Sheu, C. Y. Lee, and H. B. Lee. The study of mechanical properties and corrosion behavior of the Fe-based

amorphous alloy coatings using high velocity oxygen fuel spraying. *Journal of Alloys and Compounds*, Vol. 867, 2021, id. 159132.

[13] Zhou, Z. Y., B. Liu, W. M. Guo, A. Fu, H. Duan, and W. H. Li. Corrosion behavior and mechanism of FeCrNi medium entropy alloy prepared by powder metallurgy. *Journal of Alloys and Compounds*, Vol. 867, 2021, id. 159094.

[14] Chang, J. H., J. M. Chou, R. I. Hsieh, and J. L. Lee. Corrosion behaviour of an alloy formed by inductive melting of a cobalt-based alloy and AISI 4140 steel. *Corrosion Science*, Vol. 51, No. 5, 2009, pp. 987–996.

[15] Wang, J. Y., W. H. Li, H. L. Yang, H. Huang, S. X. Ji, and J. M. Ruan. Corrosion behavior of CoCrNi medium-entropy alloy compared with 304 stainless steel in H_2SO_4 and NaOH solutions. *Corrosion Science*, Vol. 177, 2020, id. 108973.

[16] Thorhallsson, A. I., I. Csáki, L. E. Geambazu, F. Magnus, and S. N. Karlsdottir. Effect of alloying ratios and Cu-addition on corrosion behaviour of CoCrFeNiMo high-entropy alloys in superheated steam containing CO_2, H_2S and HCl. *Corrosion Science*, Vol. 178, 2021, id. 109083.

[17] Liu, J., H. Liu, X. H. Tian, H. F. Yang, and J. B. Hao. Microstructural evolution and corrosion properties of Ni-based alloy coatings fabricated by multi-layer laser cladding on cast iron. *Journal of Alloys and Compounds*, Vol. 822, 2020, id. 153708.

[18] Oliveira, A. B., A. C. Bastos, C. M. Fernandes, C. M. S. Pinho, A. M. R. Senos, E. Soares, et al. Corrosion behaviour of WC–10% AISI 304 cemented carbides. *Corrosion Science*, Vol. 100, 2015, pp. 322–331.

[19] Masoud, S., D. S. Mersagh, and F. S. Moeini. Deposition of Ni-tungsten carbide nanocomposite coating by TIG welding: Characterization and control of microstructure and wear/corrosion responses. *Ceramics International*, Vol. 44, No. 18, 2018, pp. 22816–22829.

[20] Hochstrasser, S., Y. Mueller, C. Latkoczy, S. Virtanen, and P. Schmutz. Analytical characterization of the corrosion mechanisms of WC-Co by electrochemical methods and inductively coupled plasma mass spectroscopy. *Corrosion Science*, Vol. 49, No. 4, 2007, pp. 2002–2020.

[21] Kim, K. H., S. H. Lee, N. D. Nam, and J. G. Kim. Effect of cobalt on the corrosion resistance of low alloy steel in sulfuric acid solution. *Corrosion Science*, Vol. 53, No. 11, 2011, pp. 3576–3587.

[22] Chen, S. F., S. Y. Liu, Y. Wang, X. G. Sun, Z. W. Zou, X. W. Li, et al. Microstructure and Properties of HVOF-Sprayed NiCrAlY Coatings Modified by Rare Earth. *Journal of Thermal Spray Technology*, Vol. 23, No. 5, 2014, pp. 809–817.

[23] Yang, F., J. Guo, F. C. Xiu, L. Yang, and Z. H. Gao. Effect of Nb and CeO_2 on the mechanical and tribology properties of Co-based cladding coatings. *Surface and Coatings Technology*, Vol. 288, 2016, pp. 25–29.

[24] Hu, Z. L., Q. Pang, G. Q. Ji, and G. H. Wu. Mechanical behaviors and energy absorption properties of Y/Cr and Ce/Cr coated open-cell nickel-based alloy foams. *Rare Metals*, Vol. 37, No. 008, 2018, pp. 650–661.

[25] Guo, D. and C. T. Kwok. Effect of pH on the corrosion behavior of tungsten-copper alloys. *Corrosion Science*, Vol. 177, 2020, id. 108994.

[26] Yin, M. Y., Z. Li, Z. Xiao, Y. Pang, Y. P. Li, and Z. Y. Shen. Corrosion behavior of Cu-Al-Mn-Zn-Zr shape memory alloy in NaCl solution. *Transactions of Nonferrous Metals Society*, Vol. 31, No. 4, 2021, pp. 1012–1022.

[27] Saud, S. N., E. Hamzah, T. Abubakar, H. R. Bakhsheshi-Rad, M. Zamri, and M. Tanemura. Effects of Mn Additions on the Structure, Mechanical Properties, and Corrosion Behavior of Cu-Al-Ni Shape Memory Alloys. *Journal of Materials Engineering and Performance*, Vol. 23, No. 10, 2014, pp. 3620–3629.

[28] Tobar, M. J., C. Álvarez, J. M. Amado, G. Rodríguez, and A. Yáñez. Morphology and characterization of laser clad composite NiCrBSi-WC coatings on stainless steel. *Surface and Coatings Technology*, Vol. 200, No. 22–23, 2006, pp. 6313–6317.

[29] Cho, J. E., S. Y. Hwang, and K. Y. Kim. Corrosion behavior of thermal sprayed WC cermet coatings having various metallic binders in strong acidic environment. *Surface and Coatings Technology*, Vol. 200, No. 8, 2006, pp. 2653–2662.

[30] Bartkowski, D., A. Młynarczak, A. Piasecki, B. Dudziak, M. Gościański, and A. Bartkowska. Microstructure, microhardness and corrosion resistance of Stellite-6 coatings reinforced with WC particles using laser cladding. *Optics & Laser Technology*, Vol. 68, 2015, pp. 191–201.

[31] Fan, L., H. Y. Chen, Y. H. Dong, X. Y. Li, L. H. Dong, and Y. S. Yin. Corrosion behavior of fe-based laser cladding coating in hydrochloric acid solutions. *Acta Metallurgica Sinica*, Vol. 54, No. 07, 2018, pp. 1019–1030.

[32] Masoud, S., D. S. Mersagh, and F. S. Moeini. Deposition of Ni-tungsten carbide nanocomposite coating by TIG welding: Characterization and control of microstructure and wear/corrosion responses. *Ceramics International*, Vol. 44, No. 18, 2018, pp. 22816–22829.

[33] Sabzi, M., S. Mersagh Dezfuli, and S. M. Mirsaeedghazi. The effect of pulse-reverse electroplating bath temperature on the wear/corrosion response of Ni-Co/tungsten carbide nanocomposite coating during layer deposition. *Ceramics International*, Vol. 44, No. 16, 2018, pp. 19492–19504.

[34] Parisa, F. and K. Radovan. Corrosion and wear behavior of laser cladded Ni-WC coatings. *Surface and Coatings Technology*, Vol. 276, 2015, pp. 121–135.

[35] Fu, A. Q. and Y. F. Cheng. Characterization of corrosion of X65 pipeline steel under disbonded coating by scanning Kelvin probe. *Corrosion Science*, Vol. 51, No. 4, 2009, pp. 914–920.

[36] Tsay, L. W., H. L. Lu, and C. Chen. The effect of grain size and aging on hydrogen embrittlement of a maraging steel. *Corrosion Science*, Vol. 50, No. 9, 2008, pp. 2506–2511.

[37] Zhu, J., L. Xu, M. Lu, L. Zhang, and W. Chang. Interaction effect between $Cr(OH)_3$ passive layer formation and inhibitor adsorption on 3Cr steel surface. *RSC Advances*, Vol. 5, No. 1, 2015, pp. 18518–18522.